Author Manuscript

Ultrasmall High-Entropy-Alloy Nanozyme Catalyzed *In Vivo* ROS and NO Scavenging for Anti-Inflammatory Therapy

Daeeun Choi, Yeonju Boo, Seonhye Park, Liangliang Xu, Seongbeen Kim, Seung Yeop Yi, Sangmin Lee, Ruopeng Wu, Won Jong Kim and Jinwoo Lee**

D. Choi, S. Park, Dr. L. Xu, Dr. S. Kim, S.Y. Yi and Prof. J. Lee

Department of Chemical and Biomolecular Engineering, Korea Advanced Institute of Science and Technology (KAIST), 291 Daehak–ro, Yuseong–gu, Daejeon 34141, Korea.

E–mail: jwlee1@kaist.ac.kr

This is the author manuscript accepted for publication and has undergone full peer review but has not been through the copyediting, typesetting, pagination and proofreading process, which may lead to differences between this version and the Version of Record. Please cite this article as doi: 10.1002/adhm.202402005.

This article is protected by copyright. All rights reserved.

Y. Boo, S. Lee and Prof. W. J. Kim

Department of Chemistry, Pohang University of Science and Technology (POSTECH), 77 Cheongam–Ro, Nam–Gu, Pohang, Gyeongbuk 37673, Republic of Korea.

E–mail: wjkim@postech.ac.kr

R.Wu

Department of Mathematics, College of Literature, Science, and the Arts (LSA), University of Michigan, Ann Arbor, East Hall, 530 Church Street, Ann Arbor, MI 48109

Keywords: high-entropy alloy, ROS and RNS, nanozyme, anti-inflammatory therapy

Abstract

Author Manuscript

This article is protected by copyright. All rights reserved.

Author Manuscript

High-entropy alloy (HEA) nanoparticles possess finely tunable and multifunctional catalytic activity due to their extremely diverse adsorption sites. Their unique properties enable HEA nanoparticles to mimic the complex interactions of the redox homeostasis system, which is composed of cascade and multiple enzymatic reactions. The application of HEAs in mimicking complex enzymatic systems remains relatively unexplored, despite the importance of regulating biological redox reactions. Here, we report that ultra-small (<10nm in a diameter) HEA nanozymes consisting of five platinum-group metals with tunable morphologies from planar to dendritic structures were synthesized. The synthesized HEA nanozymes exhibited higher peroxidase-like activity compared to monometallic platinum-group nanoparticles. Additionally, HEA nanoparticles effectively mimicked RONS-regulation metabolism in cascade reactions involving SOD and CAT, as well as in multiple reactions including HORAC and NO scavenging. As a result, the HEA nanozyme exhibited superior anti-inflammatory efficacy both *in vitro* and *in vivo*. Our findings underscore the effectiveness of the high-entropy alloy structure in restoring *in*

This article is protected by copyright. All rights reserved.

Author Manuscript

vivo enzymatic systems through intrinsic activity enhancements and cascade reaction mechanisms.

1. Introduction

Reactive Oxygen and Nitrogen Species (RONS), which are radical derivatives of molecular oxygen and nitrogen including NO, •OH, H_2O_2, and $O_2^{\bullet-}$. [1] They are essential for regulating signaling pathways at low concentrations, but excessive RONS production in inflammatory diseases not only induce tissue damage and apoptosis but also function as proinflammatory mediators that enhance the invasion of immune cells and their secretion of inflammatory agents. [2] Variety of enzymes, such as superoxide dismutase (SOD), catalase (CAT) and peroxidase (POD), exist in living organisms to maintain RONS homeostasis in physiological state. [3] Unfortunately, additional treatment is required to regulate the excessively expressed RONS in pathological conditions.

This article is protected by copyright. All rights reserved.

Author Manuscript

Nanozymes, nanomaterials with intrinsic enzyme-like activity, have been vigorously studied to overcome the disadvantages of natural enzymes. Among diverse types of nanozyme, RONS scavenging nanozyme have been intensively used in anti-inflammation therapy to support the inherent enzyme system. One conventional approach is combining multiple reaction capabilities, which highlight a synergistic effect of cascade reactions including SOD, CAT and POD. [4] When the active sites are positioned in close proximity at the nanoscale, it enables the synergistic cascade reaction with serial RONS elimination. Another strategy focuses on enhancing the catalytic performance for a single reaction to improve therapeutic efficiency. [5] By tuning the active sites of the catalyst, it is possible to modulate the reaction mechanism and reduce the energy barrier. However, RONS scavenging nanozymes that combine both multiple reaction activity and catalyst engineering have been rarely studied to date.

Recently, High-entropy alloy (HEA) nanoparticles have received great attention in the field of catalyst, due to their tunable and multifunctional catalytic activities. [6] At least five elements are homogeneously and randomly mixed in the HEA nanoparticles, which

This article is protected by copyright. All rights reserved.

Author Manuscript

are called complete solid-solution state. The random distribution of various elements in HEA nanoparticles creates unique and distinct surface atoms, resulting in a nearly continuous d-band spectrum through electronic hybridization. This leads to a vast array of diverse active sites, significantly broadening the design space for catalysts with desirable activity and selectivity. [7] Therefore, HEA nanoparticles stand for an optimal RONS scavenging nanozyme platform, capable of synergistic removal of various RONS through cascade reactions and enhancement of specific reaction activities through catalyst design. Nonetheless, reports on HEA-based RONS scavenging nanozymes for anti-inflammatory therapy have been exceedingly scarce.

Herein, we report on ultra-small colloidal HEA nanozymes composed of five metals (Ru, Rh, Pd, Ir, Pt), synthesized using a dropwise hot injection method. By adjusting the concentration of hydrochloric acid in the metal precursors, we controlled the surface morphology of the particles from planar (PHEA) to dendritic (DHEA) forms. When comparing POD performance, the specific activity of PHEA nanozyme was found to be 311 U/μmol, 3.7-fold higher than that of monometallic platinum nanozyme.

This article is protected by copyright. All rights reserved.

Author Manuscript

Additionally, a steady-state kinetic parameter analysis based on particle morphology revealed that PHEA is the most suitable structure for therapeutic application. PHEA also exhibited remarkable performance in cascade reactions involving SOD and CAT, as well as in multiple reactions including hydroxyl radical antioxidant capacity (HORAC) and NO scavenging. Consequently, PHEA demonstrated superior RONS and pro-inflammatory cytokine inhibition rates in both *in vitro* and *in vivo* using a peritonitis model. In this study, we present a rational design of high-entropy alloy nanozymes optimized for anti-inflammation therapy.

2. Results and Discussion

A schematic illustration of three types of nanozyme is shown with brief explanations in **Figure 1a**: monometallic nanoparticles (Mono), planar high-entropy alloy nanoparticles (PHEA), and dendritic high-entropy alloy nanoparticles (DHEA). Unlike conventional metal nanoparticle synthesis, we injected the mixed metal precursor

This article is protected by copyright. All rights reserved.

Author Manuscript

solution into a preheated colloidal stabilizer and polyol solution to obtain complete solid-solution nanoparticles. Poly(vinylpyrrolidone) (PVP, M_w = 40,000) was employed as a stabilizer owing to its excellent thermal stability, while triethylene glycol (TEG) served as a reducing agent and a solvent due to its high boiling point. Five elements (Ru, Rh, Pd, Ir, Pt) with similar atomic radii were selected due to increase the entropy term in the mixing energy (**Figure S1**). Furthermore, these platinum-group metals have been widely used in RONS scavenging nanozyme given their high intrinsic catalytic activity. The metal precursor aqueous solutions were added dropwise to prevent the formation of phase-separated alloys attributed to the different reduction potentials of each metal ion. This dropwise strategy allows the concentration of each metal ion to reach a steady state and remain constant during the growth of the nanoparticles. [8] Furthermore, we demonstrated that the morphology of HEA nanoparticles could be tuned to a dendritic structure by adjusting the pH using HCl. Monometallic Pt nanoparticles (Mono Pt) were also synthesized for a control group. The detailed synthesis method can be found in the Methods section of the Supporting Information.

This article is protected by copyright. All rights reserved.

Author Manuscript

The bright-field transmission electron microscopy (TEM) image (**Figure S2**) showed that the synthesized PHEA particles have a uniform size distribution and quasi-spherical morphology with a planar surface. Energy dispersive spectrometry (EDS) demonstrated that each metal element (Ru, Rh, Pd, Ir, Pt) within a particle is randomly and homogeneously dispersed, as shown in **Figure 1b**. Given that elements with diverse redox potentials and atomic radii typically form phase separated structures (e.g. core-shell, Janus), [9] the formation of this single-phase solid-solution alloy indicates the effectiveness of the synthesis strategy. The aberration-corrected HAADF-STEM image of PHEA revealed a particle d-spacing of 0.23 nm with (111) facets, a characteristic feature of a face-centered cubic (FCC) structure (**Figure 1c**). [10] Additionally, the X-ray diffraction (XRD) pattern of PHEA exhibited two peaks at 40.4° for the (111) plane and 46.9° for the (200) plane corresponding to the FCC structure (**Figure 1d** and **Table S1**). As shown by the vertical lines in **Figure 1d** and **Figure S4a**, the presence of a unique and singular peak indicates that PHEA exists in a single phase and that the lattice parameters of the constituent elements are distorted due to alloying. The bulk content of each element in

This article is protected by copyright. All rights reserved.

Author Manuscript

the synthesized PHEA was confirmed to be around 20% by Inductively Coupled Plasma Optical Emission Spectrometry (ICP-OES) (**Figure 1e** and **Table S2**). These results suggest that the equimolar metal species are homogeneously distributed within the FCC structured PHEA nanoparticles.

Interestingly, we discovered that the addition of HCl to the metal precursor solution induced a morphological change from single-crystalline particles with a planar surface to polycrystalline particles with a dendritic morphology. We experimentally observed that the addition of 5 mM HCl resulted in the formation of visually discernible dendrimers (dendritic high-entropy alloy, DHEA). Increasing the concentration of HCl further increased the size of the dendritic particles (large-size DHEA, DHEA-L). According to XRD analysis, the crystallite size of (111) plane of DHEA is 4.86 nm which is slightly larger than 4.07 nm of PHEA (**Figure S4b** and **Table S1**). However, the particle size of DHEA observed in the TEM image is 15.4 nm which is three-fold larger than that of PHEA (**Figure 1f** and **g**). This difference suggests that the introduction of HCl does not merely increase the size of the crystals but promotes the aggregation of smaller crystals

This article is protected by copyright. All rights reserved.

Author Manuscript

into the dendrimers. Considering the origin of dendrimer formation, metal atoms that adsorb favorably to specific sites on the seed subsequently diffuse to the remaining areas of the particle surface. [11] If the rate of deposition (V_{dep}) is slower than the rate of diffusion (V_{diff}), conformal deposition occurs, forming particles with a planar surface. Otherwise, the V_{dep} is faster than the V_{diff}, continuous deposition occurs at specific sites, leading to the pile-up of metal atoms and the formation of dendritic particles. Since the V_{diff} is strongly related to the reaction temperature, adding HCl could increase the ratio of V_{dep}/V_{diff} with enhancing V_{dep} and induce DHEA synthesis.

The electronic structure and the composition of metal elements in PHEA were analyzed by X-ray photoelectron spectroscopy (XPS), a surface-sensitive probe. In the binding energy (BE) range of 60–80 eV, the doublets of core-level spectra (4f orbitals) originating from Pt and Ir were observed (**Figure 2a**). The doublets of core-level spectra (3d orbitals) of Ru, Rh, and Pd were also observed in the BE range of 270–350 eV (**Figure 2b**). The peak position and area for the $4f_{7/2}$ and $3d_{5/2}$ orbitals of each element were determined through fitting (**Figure S8**). The surface composition of PHEA was similar to

This article is protected by copyright. All rights reserved.

Author Manuscript

that obtained by ICP-OES analysis, suggesting that the surface and bulk composition of PHEA were maintained homogeneously (**Figure 1e** and **Table S2**). The position of each peak matched the previously known peak positions of bulk metal species (**Table S3**), indicating that surface of the synthesized PHEA remained in a metallic state without oxidation by the atmosphere. Additionally, the valence band (VB) spectrum of metallic species provides information about the orbital structure. Monometallic nanoparticles larger than 2 nm have characteristic peaks in the BE range of 0–6 eV, which originate from the bulk metal spectrum. [12] This characteristic peak was observed at the 5-eV region in Mono Pt, while PHEA exhibited no characteristic peak, resulting in a "featureless" VB spectrum (**Figure 2c** and **Figure S9**). This type of VB spectrum is caused by orbital hybridization among the five metal elements, [13] indicating that the elements were well-mixed in the surface of PHEA.

X-ray absorption spectroscopy (XAS) analysis was utilized to obtain more detailed information about the total atomic and electronic structure of the PHEA. In **Figure 2d–h**, the X-ray absorption near-edge structure (XANES) spectra for Ru, Rh, Pd, Ir and Pt in

This article is protected by copyright. All rights reserved.

Author Manuscript

PHEA are shown with their metallic reference foils. Normally, in the XANES spectra, an oxidation state of metal species could be estimated by the position and the intensity of absorption edge. [14] The similarity of each element's absorption edge to that of the metallic foil indicates that all elements in PHEA exist in the metallic state (M^0). Furthermore, the post-edge spectra of each metal element and the foil references have similar shape and oscillation, [15] which indicates the geometrical structure of metal elements in PHEA is similar to that of the metallic foil.

In addition, the Fourier-transformed extended X-ray absorption fine structure (FT-EXAFS) spectra of the Pt L-edge in PHEA, Mono Pt, and Pt reference foil were analyzed to obtain the coordination environment and bond length of Pt atoms (**Figure 2i**). Alloying smaller metal elements (Ru, Rh, Pd, and Ir) with Pt induces the appearance of a unique peak at a shorter range (around 2.1 Å), which is not observed in either Mono Pt or the reference foil. This peak suggests that smaller metal atoms with shorter atomic radii replaced Pt atoms during the alloying process. [16] Furthermore, the coordination environment of the five metal components of PHEA was investigated using the FT-EXAFS

This article is protected by copyright. All rights reserved.

Author Manuscript

spectra (**Figure S10**). The FT-EXAFS spectra of 4d and 5d atoms in monometallic particles should be significantly different due to their distinct atomic radii. However, in the case of PHEA, the FT-EXAFS spectra of each metal element tend to become similar. These results indicate that the five metallic elements are homogeneously mixed, forming random bonds in PHEA.

The accumulation of excessive hydrogen peroxide (H_2O_2) can lead to cellular damage and inflammation, necessitating efficient removal mechanisms. POD-catalyzed reactions play a pivotal role in RONS homeostasis by reducing H_2O_2 to water while oxidizing substrates such as glutathione (GSH). [17] As shown in **Figure 3a**, a colorimetric assay employing 3,3',5,5'-tetramethylbenzidine (TMB) was utilized to assess the catalytic efficiency of peroxidase. In the presence of POD, the reaction of TMB with H_2O_2 results in the formation of a blue-colored oxidized TMB. The TMB-based colorimetric analysis is notable for its high sensitivity among colorimetric substrates, which enables real-time monitoring with high accuracy. [18] For this reason, the POD reaction was adopted to compare the performance of nanozymes.

This article is protected by copyright. All rights reserved.

Author Manuscript

The POD-like activity of the HEA nanozymes was quantified by plotting the time course of the absorbance intensity at 652 nm of oxidized TMB. All experiments were conducted under weakly acidic conditions (pH 6.0) using a 0.1 M phosphate buffer to simulate the environment of peritonitis model. Mono Pt (the control group) was widely used in RONS scavenging nanozyme due to moderate O-binding energy and high catalytic performance. [19] As shown in **Figure S11**, PHEA exhibited the highest POD-like activity, followed by DHEA and Mono Pt under identical condition. The specific activity (SA) values [20] of nanozymes were calculated to quantify POD performance under substrate saturated condition (**Figure 3b**). SA of PHEA was 311 U/mmol, which was 1.2–fold higher than that of DHEA and 3.7–fold higher than that of Mono Pt. The higher performance of PHEA compared to DHEA is attributable to the formation of enlarged particles of DHEA, which diminishes the number of exposed active sites, thereby reducing molar activity. This suggests that PHEA is the optimal choice for *in vivo* peritonitis therapy, where high therapeutic effectiveness at low doses is crucial. To ascertain the role of the HEA structure, the performance of five Mono (Ru, Rh, Pd, Ir, Pt) nanzyme mixture

This article is protected by copyright. All rights reserved.

Author Manuscript

(in **Figure S3**) was evaluated under the identical substrate and nanozyme concentrations. As shown in **Figure S12**, PHEA demonstrated superior performance in comparison to the physically mixed Mono nanozymes. This result highlights that the electronic structure modification of active sites through high-entropy alloying is as important as introducing various metal elements.

A steady-state kinetic assay was performed to determine the kinetic parameters of the nanozymes. As illustrated in **Figures 3c** and **Figure S13**, the HEA and Mono Pt nanozymes exhibited Michaelis-Menten kinetics with respect to TMB and H_2O_2. For the substrate TMB, PHEA exhibited the highest k_{cat} (8.65 s^{-1}), which was 1.5–fold and 5.2–fold greater than that of DHEA (k_{cat}=5.75 s^{-1}) and Mono Pt (1.66 s^{-1}). The K_M values for PHEA (0.14 mM) and DHEA (0.13 mM) are comparable, twice larger than that of Mono Pt (0.06 mM). Furthermore, the k_{cat}/K_M value of PHEA were the highest at 5.97×10^4 $M^{-1}s^{-1}$, which is 1.35–fold and 2.19–fold greater than those of DHEA and Mono Pt. PHEA also displayed the highest k_{cat} and k_{cat}/K_M values for the H_2O_2 substrate, indicating the advantage of PHEA *in vivo* therapy, where TMB is absent. To compare the kinetic parameters of PHEA

This article is protected by copyright. All rights reserved.

Author Manuscript

with the previously reported materials, k_{cat} and K_M values are displayed in **Figure S14** and **Table S4**. The calculation criterion of enzyme concentration was converted from the atom concentration ($[E_{/metal}]$) to the particle concentration ($[E/_{particle}]$) to unify calculation units. Among various materials, our PHEA showed the highest k_{cat} of 2.98×10^4 s^{-1} and the comparable K_M of 1.4×10^{-4} M. The origin of the elevated POD activity of HEA nanozymes compared to Mono Pt could be explained by the d-band theory. Following the Sabatier principle, the optimal catalytic activity requires active sites that provide an ideal binding strength with the intermediates. In transition metals, the d orbitals predominantly contribute to this binding, and thus, tuning the average energy level of the d-band is crucial. [21] Consequently, through high-entropy alloying, the d-band of the catalyst could be fine-tuned in a more favorable direction, which enhanced the POD activity.

Interestingly, the k_{cat} values of DHEA are 2.31–fold higher than that of PHEA when calculating the [E] value based on the surface atom concentration ($[E_{/surface}]$, **Table S4a**). The nanodendrite structure of metal nanoparticles is known to increase the proportion of low-coordination number atoms on the catalyst surface, thereby enhancing

This article is protected by copyright. All rights reserved.

Author Manuscript

the intrinsic activity of metal active sites. [22] The results suggest that the correlation between surface morphology and intrinsic activity is also applicable to the HEA nanozymes. The k_{cat} and k_{cat}/K_M values of DHEA are also higher than those of PHEA when considering each particle as a single enzyme (**Table S4b**). This implies that DHEA could be more advantageous than PHEA for applications such as enzyme-linked immunosorbent assay (ELISA), where a limited number of particles are used. [23] However, it is crucial to minimize the amount of metal used to reduce toxicity and side-reaction in *in vivo* anti-inflammation therapy. [24] As a result, PHEA, which has the highest catalytic performance per total usage of metal, was adapted to further analysis. Additionally, we evaluated the stability of PHEA with multiple methods. First, as shown in **Figure S15a**, PHEA exhibited significantly superior thermal stability compared to the natural enzyme HRP at 50°C. Furthermore, as shown in **Figure S15b**, PHEA retained 96% of its initial performance even after being stored under ambient conditions for six months, demonstrating only a 4% decrease compared to its performance immediately after

This article is protected by copyright. All rights reserved.

Author Manuscript

synthesis. This demonstrates the high stability of PHEA, which is attributed to the high-entropy alloying effect.

To counteract the harmful effects of RONS, cells have evolved an intricate antioxidant defense system. [1] One key component of this defense system is the multiple and cascade reactions including SOD, CAT and POD. This cascade reaction starts with SOD, which converts $O_2^{\cdot-}$ into H_2O_2 or O_2. H_2O_2 is sequentially broken down by CAT and POD into H_2O or O_2. This sequential RONS elimination process within the body was effectively mimicked by PHEA due to its diverse and appropriate active sites (**Figure 3d**).

CAT-like activity was measured in two ways with the production of oxygen molecules and the reduction of hydrogen peroxide over time. [5a, 25] **Figure S16** showed the O_2 generation rates at varying PHEA concentrations in 0.1M phosphate buffer (pH 6.0). The result demonstrates that PHEA exhibits concentration-dependent CAT-like activity. Furthermore, the CAT-like specific activity of PHEA was evaluated by monitoring the 240 nm absorbance of H_2O_2. As shown in **Figure 3e**, in the absence of a catalyst, the

This article is protected by copyright. All rights reserved.

Author Manuscript

H_2O_2 concentration remained constant over time. In contrast, in the presence of PHEA, the concentration decreased to 20% of its original value within 10 minutes, and the measured SA of PHEA was 17.6 U/μmol. The formation of O_2 and the reduction of H_2O_2 indicate that PHEA scavenges H_2O_2 through CAT-like activity. DHEA presented the 14.4 U/μmol of SA through the reduction of H_2O_2. (**Figure S17**). The SOD-like activity of PHEA was quantified using a commercial SOD assay kit which monitors the capability to eliminate $O_2^{\cdot-}$ using xanthine (X), xanthine oxidase (XO) and WST-1 in **Figure 3f**. As the concentration of PHEA increased to 0.333 mg/mL, the inhibition rate against $O_2^{\cdot-}$ radicals reached 100%, indicating the apparent SOD-like activity. The SA of PHEA was calculated using the inhibition rate, resulting in a value of 377 U/mol. The specific activity of the SOD-like reaction for DHEA was quantified at 183 U/mol, lower than that of PHEA (**Figure S18**).

In addition, the terephthalic acid (TA) assay was combined with the Fenton reaction of Fe^{2+} and H_2O_2 to assess the HORAC of PHEA. [26] Fenton reaction generates ·OH and oxidizes TA to 2-hydroxyterephthalic acid (TAOH), which emits fluorescence at

This article is protected by copyright. All rights reserved.

Author Manuscript

440 nm. As shown in **Figure 3g**, the fluorescence exhibited a notable decrease as the concentration of PHEA was elevated, suggesting that the in situ generated ·OH from H_2O_2 decomposition was effectively quenched. A comparable reduction in fluorescence was observed in DHEA, indicating that DHEA also possesses HORAC activity (**Figure S19**). NO-scavenging ability of the nanozymes was further assessed using a solution containing 25 μM N-diazeniumdiolates-incorporated pyrrolidine (Py-NO), NO releasing agent. [27] The remaining NO were significantly reduced by both PHEA and DHEA in a concentration-dependent manner, and PHEA showed slightly better NO scavenging ability (**Figure S20**). These results suggest that the RONS elimination mechanism *in vivo* was effectively replicated on the highly diverse active sites of PHEA. This includes the cascade reactions of SOD and CAT, as well as the multi-enzyme activities of HORAC and NO elimination. Furthermore, PHEA exhibited higher RONS elimination efficacy than DHEA at identical doses, implying that PHEA is a more suitable nanozyme than DHEA for *in vivo* peritonitis therapy. To elucidate the intrinsic multi-enzymatic mechanism of high-entropy alloys facilitate reactions, we conducted systematic density functional theory

This article is protected by copyright. All rights reserved.

Author Manuscript

(DFT) calculations. As shown in **Figure 3i**, the reaction free energies of Pt and high-entropy alloys indicate that the reactions are exothermic, from O_2 adsorption to H_2O formation, and can proceed spontaneously (reaction configurations are illustrated in **Figure S21**). Furthermore, in a key elementary step ($*H_2O_2 \rightarrow *OH - *OH$), the transition state (TS) energy barrier determines the ease of the reaction. The energy barrier for the high-entropy alloy is 0.363 eV, which is lower than that of the Pt alloy (0.566 eV). This confirms that the high-entropy alloy enhances catalytic reaction optimization, consistent with experimental results.

In inflammatory diseases, the overproduced RONS act as a signaling molecule in the inflammatory response, accelerating the inflammatory process. [28] Since the HEA nanozymes demonstrated excellent RONS scavenging ability, we expected that it might be an excellent option as a potent anti-inflammatory agent for treating inflammatory diseases. We selected PHEA, which exhibited the highest RONS scavenging ability per total usage of metal, and evaluated its anti-inflammatory effect by scavenging RONS *in vitro*.

This article is protected by copyright. All rights reserved.

Author Manuscript

The anti-inflammatory effect of PHEA was evaluated *in vitro* using a murine macrophage RAW 264.7 cell line stimulated with lipopolysaccharide (LPS) (**Figure 5a**). Extracellular ROS and NO levels were quantified by Amplex red assay and Griess assay, respectively. High levels of extracellular ROS and NO were released from LPS-activated RAW 264.7 cells, but PHEA effectively reduced H_2O_2 and NO levels (**Figure 5b–c**). Also, the intracellular ROS and NO levels were quantified by fluorescence microscopy using CellROX and DAF-2DA, ROS ($O_2^{\bullet-}$ and ·OH) and NO-visualizing reagent, respectively. When RAW 264.7 cells were stimulated, both ROS and NO exhibited high fluorescence intensity, which was significantly reduced following treatment with PHEA. (**Figure 5d**). In addition, pro-inflammatory cytokine levels such as IL-6 and TNF-alpha were also significantly reduced after treatment with PHEA (**Figure 5e–g**). Oxidative stress caused by high concentrations of H_2O_2 induces cytotoxicity [29] (**Figure S13**). Therefore, we confirmed the cytoprotective effect of PHEA on H_2O_2-treated RAW 264.7 cells. After 24 hours of treatment with 1 mM H_2O_2, only about 5% of the cells survived, whereas treatment with PHEA significantly inhibited the cytotoxic effect of H_2O_2 (**Figure 5g**). In

This article is protected by copyright. All rights reserved.

Author Manuscript

other words, PHEA efficiently removed intracellular RONS, restoring cell viability in a concentration-dependent manner. In conclusion, PHEA significantly reduced pro-inflammatory cytokine levels by scavenging excess ROS and NO *in vitro* and protecting cells from oxidative stress damage. As a result, PHEAs have proven to be a potential therapeutic agent for managing various inflammatory diseases.

Based on the anti-inflammatory effect of PHEA validated *in vitro*, we evaluated the *in vivo* anti-inflammatory protective effect of PHEA in LPS-induced peritonitis model. For *in vivo* experiments, the Dulbecco's phosphate buffered saline (DPBS), or PHEA were treated via intravenous injection, and then the mouse peritonitis model was induced by intraperitoneal injection of LPS. After 4 hours, the peritoneal lavage and serum were collected for monitoring inflammatory factors (**Figure 5a**). As a result, the levels of inflammatory factors including RONS and pro-inflammatory cytokines were significantly increased in both the peritoneal lavage fluid and serum after LPS treatment, indicating that peritonitis model was successfully induced. Furthermore, an increase in inflammatory factors in serum demonstrates that systemic inflammation had also been induced (**Figure**

This article is protected by copyright. All rights reserved.

Author Manuscript

5b–i). In the PHEA-treated mice, the levels of ROS and NO in both peritoneal fluid and serum were significantly reduced, consistent with RONS scavenging ability of PHEA *in vitro* (**Figure 5b–i**). Also, the pro-inflammatory cytokine levels in both peritoneal fluid and serum were significantly reduced in the PHEA-treated mice compared to the LPS-only treated mice, indicating that PHEA effectively alleviated inflammation.

Additionally, the excessive production of RONS induced by LPS leads to systemic inflammation and oxidative stress, ultimately resulting in acute liver injury. [30] To evaluate the severity of the liver injury, the liver tissues and serum were collected 12 h after LPS injection. The level of liver injury indicators including alanine aminotransferase (ALT), and aspartate aminotransferase (AST) were significantly increased in LPS-treated mice, indicating that LPS successfully induced acute liver injury. On the other hand, the levels of ALT and AST from PHEA-treated mice were significantly reduced (**Figure 5k–l**). Furthermore, histologically stained liver tissue in LPS-treated mice showed necrosis damage and the infiltration of inflammatory cells. The damaged area of liver tissue in PHEA-treated mice was reduced (**Figure 5j)**. This reduction in inflammation is attributed

This article is protected by copyright. All rights reserved.

Author Manuscript

to the scavenging of ROS and NO, key factors in the initiation of the inflammatory response and oxidative stress, by PHEA, thereby preventing the onset of inflammation. Therefore, PHEA has exhibited a significant anti-inflammatory protective effect in animal models, it holds promise as potential therapeutic agent for the treatment of various inflammatory diseases.

The biocompatibility of a material is an essential prerequisite for its biomedical applications. Consequently, *in vitro* and *in vivo* biosafety tests were conducted to confirm the biocompatibility of PHEA. The cell cytotoxicity of PHEA was evaluated against RAW 264.7 cells. As shown in **Figure 6a**, no significant cytotoxicity was observed when RAW 264.7 cells were treated with PHEA with various concentrations for 24 hours. In addition, after treatment with PHEA (200 μg mL^{-1}) for 24 h, live dead assay fluorescence imaging did not show any significant cytotoxicity, which is consistent with the results of MTT assay (**Figure 6b)**. These results indicate that PHEA is suitable for bio application *in vitro*. Also, hemocompatibility is important for systemic delivery of materials *in vivo*. Hemolysis test was performed to confirm the biocompatibility of PHEA. As shown in **Figure 6c**, the

This article is protected by copyright. All rights reserved.

Author Manuscript

hemolysis activity of PHEA (0–100 μg mL^{-1}) was quantified to be less than 1%, thereby confirming its hemocompatibility. Next, *in vivo* biocompatibility of PHEA was evaluated in mice. PHEA (5 mg kg^{-1}) was intravenously injected into healthy mice. After seven days, the serum and major organs were collected for blood biochemistry assay and histological assay. As a result, levels of biochemistry indicators reflecting liver function (ALT and AST), heart function (CK and LDH), and kidney function (BUN and Crea) in PHEA treated group exhibited no significant differences compared to the PBS treated group (**Figure 6d–f**). In addition, as shown in **Figure 6g**, no distinguishable tissue damage was observed in major organs from PHEA treated group, indicating that PHEA is suitable for biomedical application.

3. Conclusion

In this study, our goal was to develop nanozyme with high anti-inflammatory performance by efficiently mimicking the multiple and cascade RONS scavenging

This article is protected by copyright. All rights reserved.

Author Manuscript

mechanisms in the body. To achieve this, we synthesized PHEA containing five metal elements using a dropwise and hot injection method. The homogeneity of the synthesized particles was confirmed at the atomic level through the electron microscopy and the X-ray-based analysis. Additionally, we discovered that adjusting the concentration of HCl in the metal precursor solution induced the synthesis of DHEA. The $[k_{cat}/K_M]_{metal}$ value of PHEA (5.97×10^4 $M^{-1}s^{-1}$) in POD reaction was 1.5–fold and 5.2–fold higher than those of DHEA and Mono Pt, respectively. The HEA structure enhances intrinsic catalytic activity, making PHEA most suitable for *in vivo* anti-inflammation therapy. This indicates that the formation of the high-entropy alloy led to the orbital hybridization of the metals, positioning the average d-band center of the nanozyme to achieve optimal binding strength with intermediates. Furthermore, PHEA exhibited significant activity in cascade reaction composed of SOD and CAT, as well as in multiple reactions including HORAC and NO scavenging. PHEA has demonstrated significant potential as an anti-inflammatory therapeutic agent by effectively scavenging excessive ROS and NO, key mediators of inflammation, both *in vitro* and *in vivo*. Through its ability

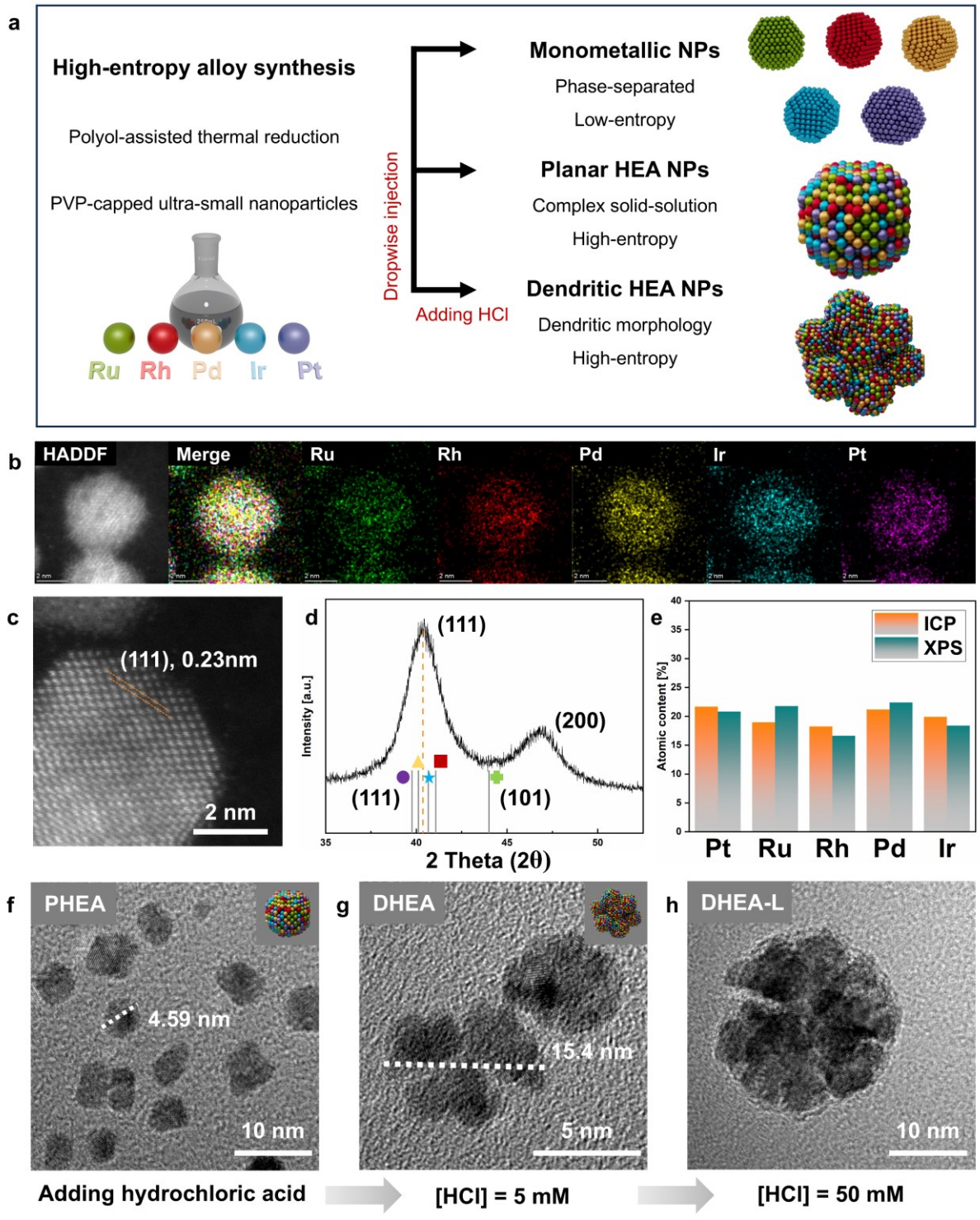
This article is protected by copyright. All rights reserved.

Author Manuscript

to reduce pro-inflammatory cytokines and alleviate oxidative stress, PHEA successfully protected cells from LPS-induced inflammation and liver injury in animal models. Furthermore, PHEA exhibited excellent biocompatibility in both *in vitro* and *in vivo* tests. In summary, our study demonstrates the successful generation of a unified catalyst platform featuring a multitude of coexisting active sites through the phenomenon of high-entropy alloying. Our catalyst effectively mimics *in vivo* enzymatic redox homeostasis systems, showcasing the potential of designing enzyme-like catalysts in diverse biomedical applications, including anti-inflammatory therapy.

This article is protected by copyright. All rights reserved.

Author Manuscript



This article is protected by copyright. All rights reserved.

Author Manuscript

Figure 1. Structural characterization of high-entropy alloy nanoparticles. (a) Schematic view of the

precursors and the synthesized monometallic, planar and dendritic high-entropy nanoparticles. **(b)** HAADF-STEM and the associated EDS mapping images of the PHEA. **(c)** Aberration-corrected atomic resolution HAADF-STEM micrograph of PHEA. **(d)** XRD pattern of PHEA in the range of 2θ = 35–55° with the reference peaks of bulk metal (purple circle: Pt, yellow triangle: Pd, blue star: Ir, red square: Rh and green cross: Ru). **(e)** Atomic content analysis data of PHEA obtained from different techniques, ICP-OES (orange) and XPS (cyan), Bright-field TEM images of **(f)** PHEA, **(g)** DHEA and **(h)** DHEA-L.

This article is protected by copyright. All rights reserved.

Author Manuscript

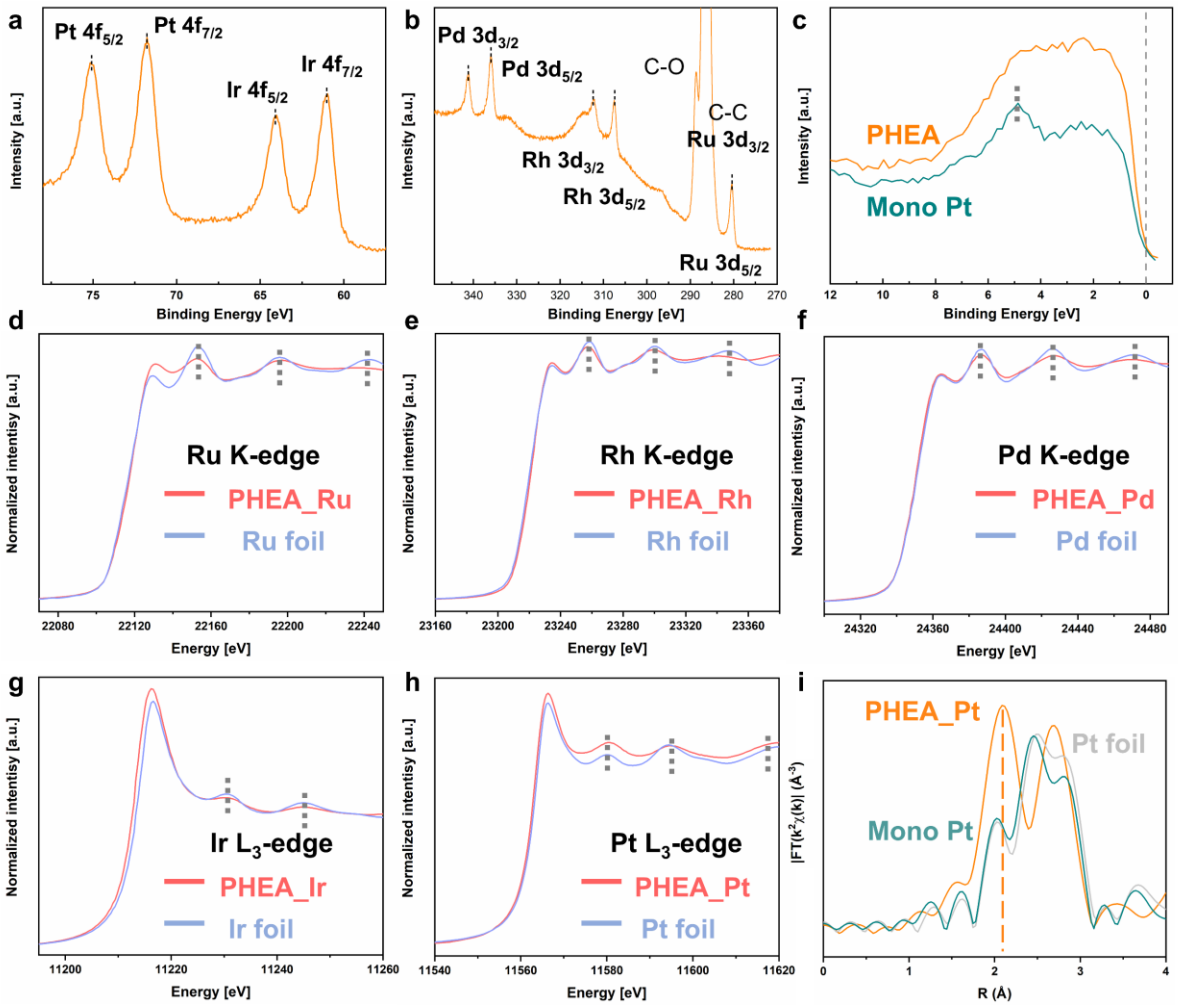


Figure 2. Electronic structure characterization of the PHEA. Core-level XPS spectra of five metal elements of PHEA in the regions of **(a)** 55–80 eV and **(b)** 270–345 eV, **(c)** Valence-band XPS spectra of PHEA and Mono Pt. XANES spectra for the **(d)** Ru K-edge, **(e)** Rh K-edge, **(f)** Pd K-edge, **(g)** Ir L_3-edge, **(h)** Pt L_3-edge (PHEA: red, Foil references: blue, characteristic oscillation: gray

This article is protected by copyright. All rights reserved.

Author Manuscript

dot lines). **(i)** FT-EXAFS spectra for Pt L_3-edge in the PHEA, Mono Pt and Pt foil reference (PHEA: orange, Mono Pt: cyan, Pt foil: gray).

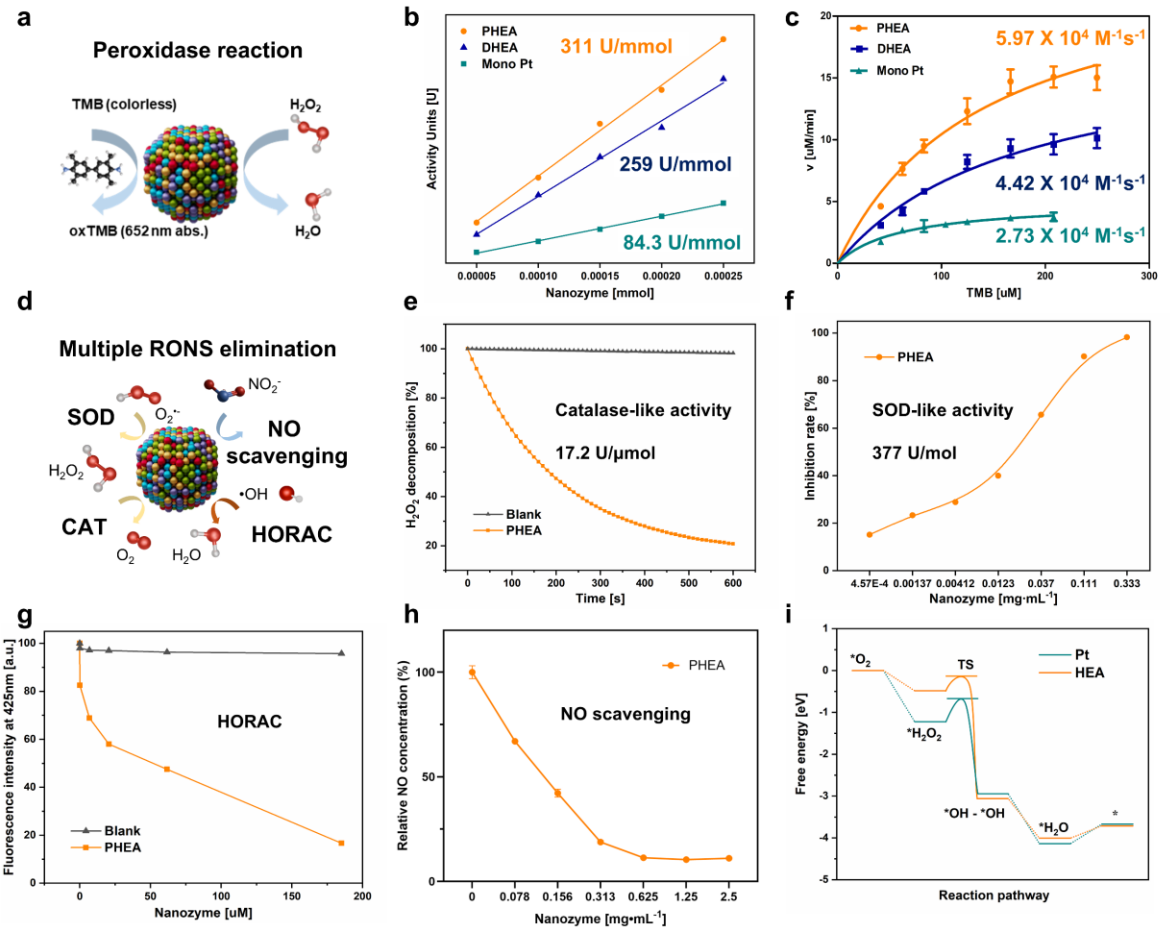


Figure 3. Assessing the peroxidase-like perfomance of nanozymes, and the standard deviation is indicated by each error bar. (a) Schematic illustration of the colorimetric peroxidase reactions using PHEA. **(b)** Determination of the specific activities of SAzymes (U mg^{-1}). One

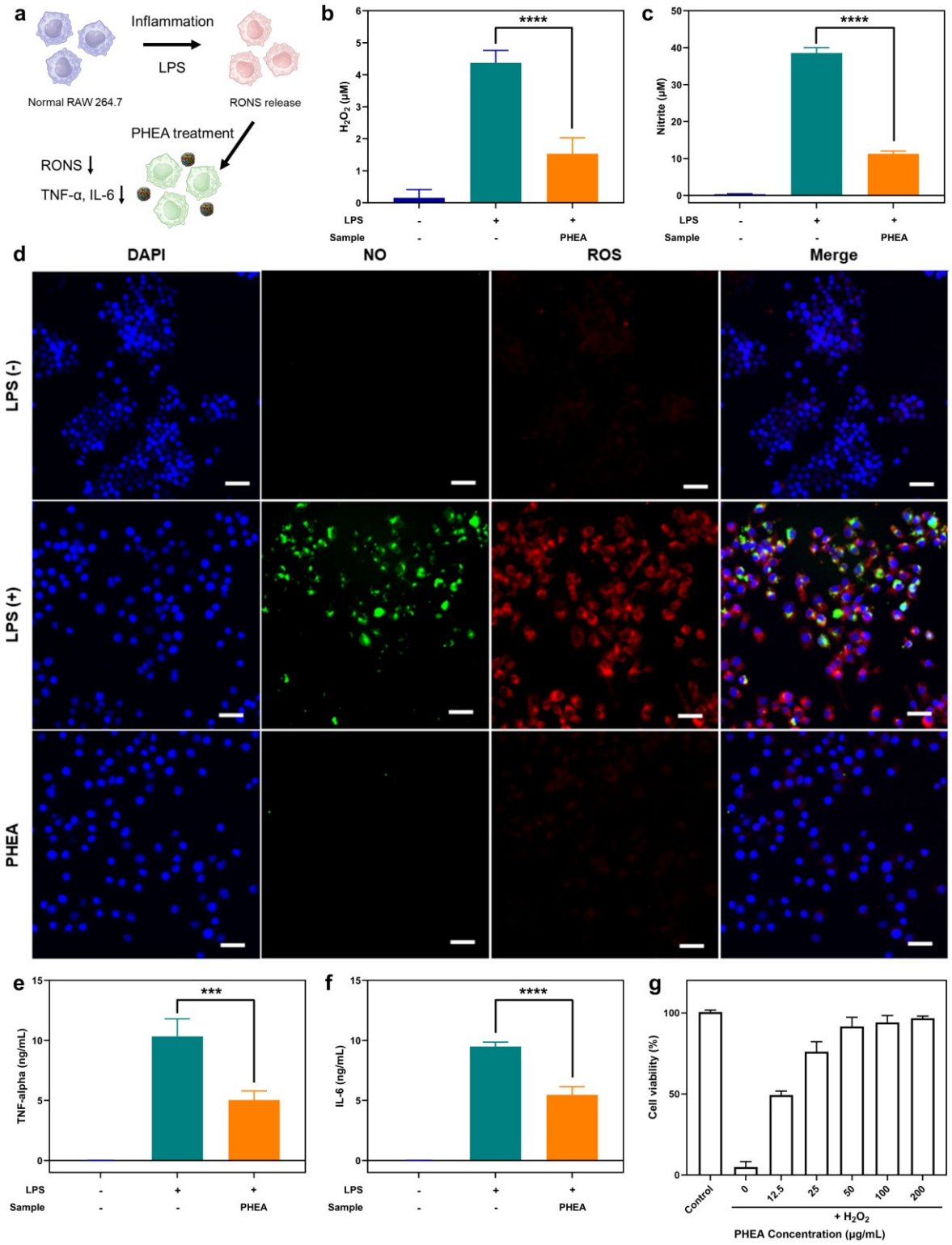
This article is protected by copyright. All rights reserved.

Author Manuscript

nanozyme activity unit (U) corresponds to the amount of nanozyme that forms one μmol of product per min. **(c)** Steady-state kinetic assay plots of nanozymes using TMB as the substrates. **(d)** Schematic illustration of RONS scavenging reactions in the PHEA. **(e)** Time-dependent absorbance (240 nm) curves of H_2O_2 generated by the catalase reaction with PHEA. **(f)** $O_2^{\bullet-}$ inhibition rate versus nanozyme concentration curve with the SOD-like activity of PHEA. **(g)** •OH inhibition of PHEA obtained from the Fenton reaction and TA. **(h)** NO scavenging activity of the PHEA with Griess assay. **(i)** The free energy diagram of Pt and high-entropy alloy with the reaction pathway.

This article is protected by copyright. All rights reserved.

Author Manuscript



This article is protected by copyright. All rights reserved.

Author Manuscript

Figure 4. Anti-inflammatory effect of PHEA Nanozyme in LPS-activated RAW 264.7 cells *in vitro*. **(a)** Schematic diagram of the *in vitro* RONS scavenging capability of PHEA. **(b)** Extracellular ROS and **(c)** NO levels of RAW 264.7 cells after treatment with PHEA. **(d)** Fluorescence microscopy images of LPS-activated RAW 264.7 cells following PHEA administration. CellROX (red), DAF-2 DA (green), and DAPI (blue) labeled intracellular ROS, NO, and nuclei, respectively. (Scale bar = 50 μm). Measurement of pro-inflammatory cytokine levels, specifically **(e)** TNF-α and **(f)** IL-6 after treatment with PHEA. **(g)** Cell viability of RAW264.7 cells exposed to 1mM H_2O_2 and various concentrations of PHEA. Data represent the mean ± SD (n = 4, ***p < 0.001, ***p < 0.0001).

This article is protected by copyright. All rights reserved.

Author Manuscript

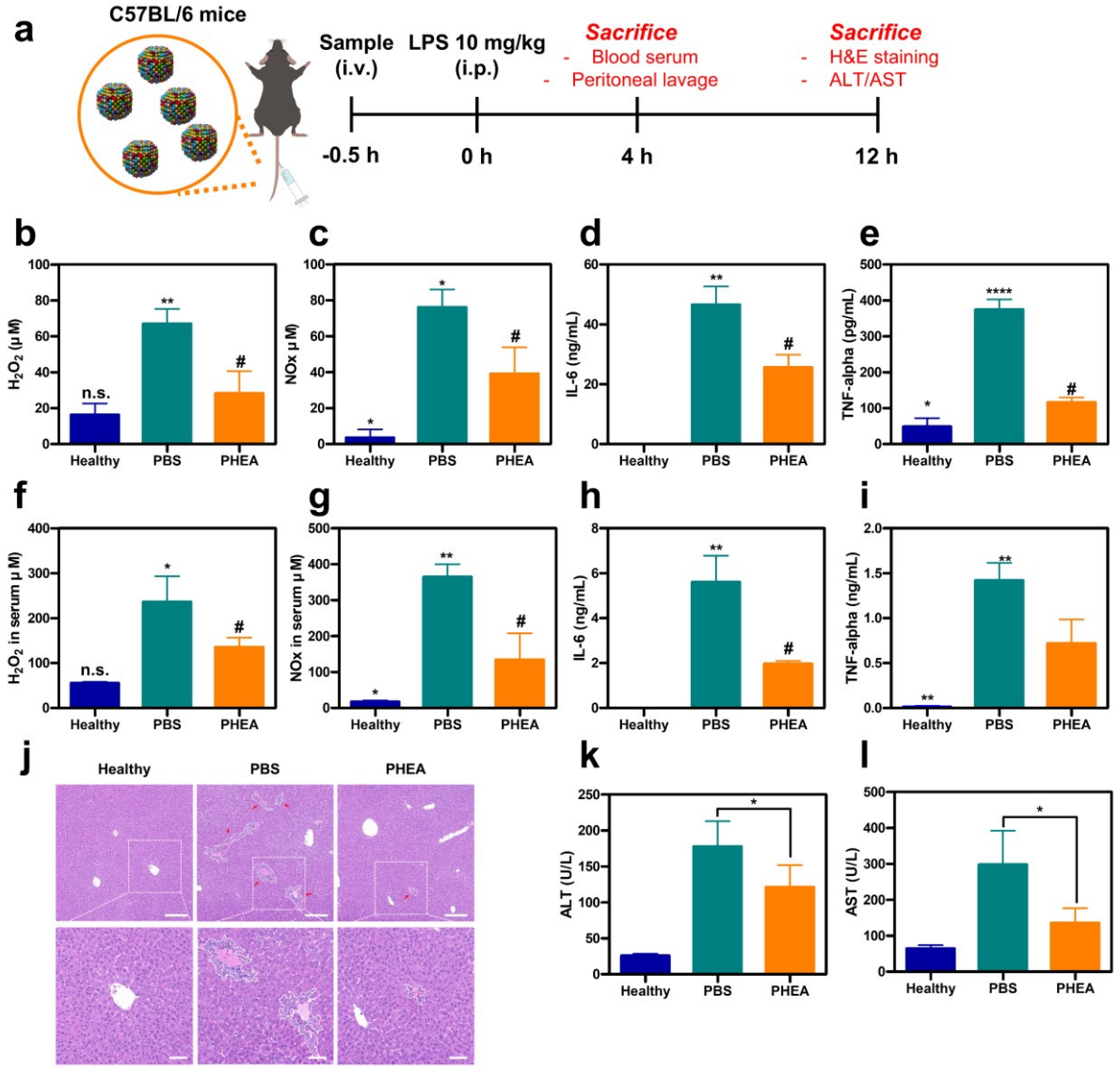


Figure 5. *In vivo* protective effect of PHEA in LPS-induced peritonitis model. (a) Overall experimental timeline for peritonitis mouse model induction and PHEA treatments. **(b)** Quantification of ROS, **(c)** NO levels and pro-inflammatory cytokine levels including **(d)** TNF-α

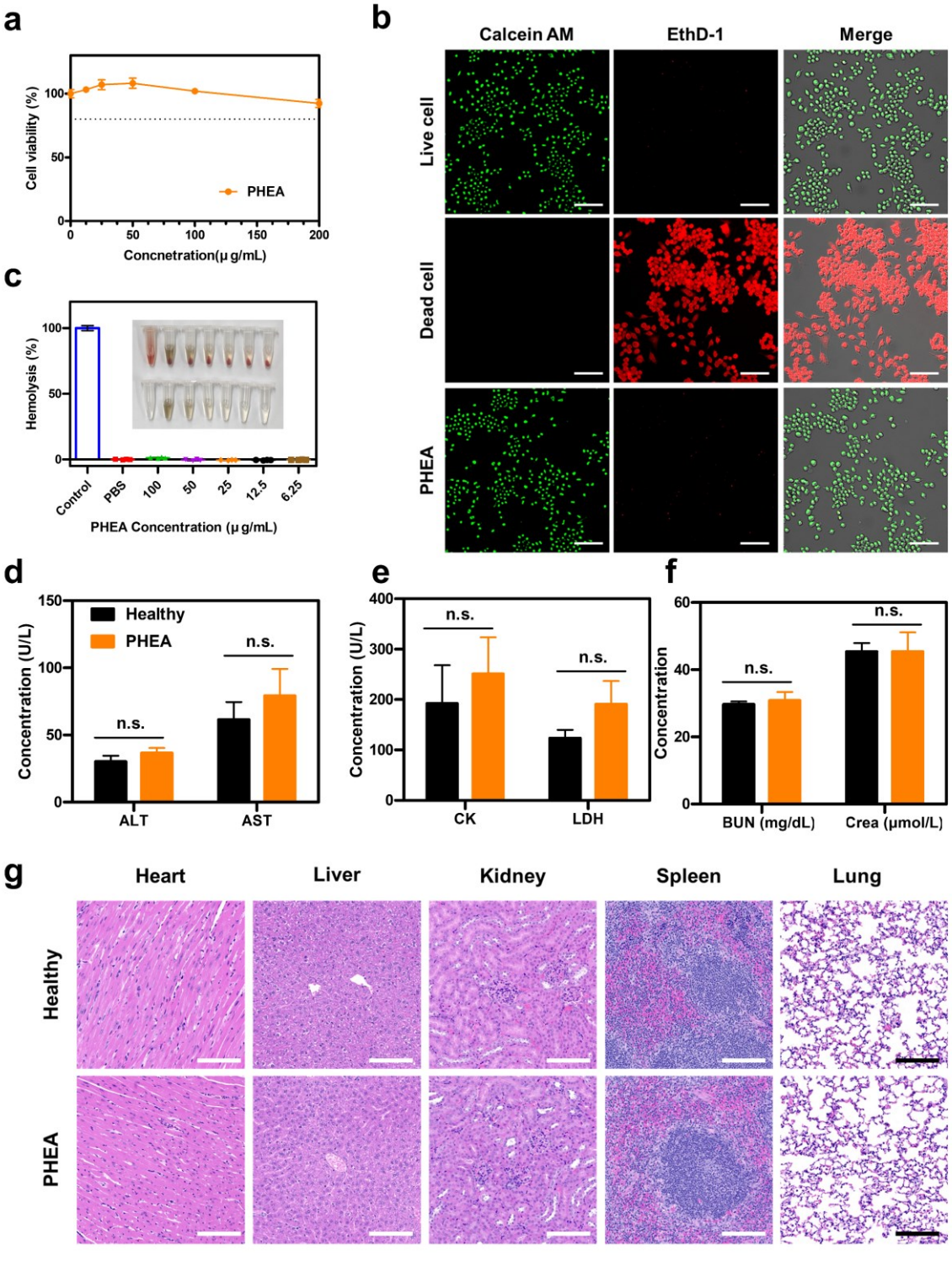
This article is protected by copyright. All rights reserved.

Author Manuscript

and **(e)** IL-6 of peritoneal lavage fluid after treatment with PHEA. **(f)** Quantification of ROS, **(g)** NO level and pro-inflammatory cytokine levels including **(h)** TNF-α and **(i)** IL-6 of serum after treatment with PHEA. **(j)** Representative H&E staining of liver tissues at 12 h after different treatments. The red arrowheads and white dotted lines outline hepatic necrosis regions and inflammatory cell foci. (Scale bars = 200 μm, full scanned images; 50 μm, enlarged images). **(k)** Quantification of liver function indicators, ALT and **(l)** AST in LPS-induced mice at 12 h after different treatments. Data represents the mean ± SD (n=3, # compared with sample groups, *p < 0.05, **p < 0.01, ****p < 0.0001).

This article is protected by copyright. All rights reserved.

Author Manuscript



This article is protected by copyright. All rights reserved.

Author Manuscript

Figure 6. Biosafety assessment of PHEA. (a) Cell viability of RAW 264.7 cells treated with various concentrations of PHEA (n=5). **(b)** Live/dead assay of Raw 264.7 cells after the treatment of PHEA. Live cells and dead cells were stained with calcein AM (green), and ethidium homodimer-1 (red), respectively (Scale bar = 50 μm). **(c)** Hemolysis test of PHEA (n=4). **(d)** Biochemical assay of the serum collected seven days after the treatment of samples. Liver function test of alanine aminotransferase (ALT) and aspartate aminotransferase (AST). **(e)** Heart function test of creatine kinase isoenzymes (CK) and lactate dehydrogenase (LDH). **(f)** Kidney function test of blood urea nitrogen (BUN) and creatinine (CREA). Data represents the mean ± SD (n=3, n.s., not significant.). **(g)** Histological assay with hematoxylin and eosin (H&E) staining of major organs collected seven days after the treatment of samples (Scale bar = 100 μm).

4. Experimental Section

Synthesis of PHEA: Using a previously reported method with a slight modification, PHEA was synthesized. [31] First, 5 mmol of PVP and 150 mL of TEG were completely mixed in a 250mL three-necked flask. Next, the flask and the solution were degassed (condition: at

This article is protected by copyright. All rights reserved.

Author Manuscript

80℃, for 1 hour, with 600 rpm stirring). After an argon backfill, the PVP/TEG mixture was pre-heated to 240℃ under continuous argon flow (200 cm^3/min). While heating of the PVP/TEG solution, an equimolar mixture of five metal precursors (total amount: 0.25 mmol) was prepared using water (total volume: 10mL). Each metal precursor was either absent or chelated with potassium ions for the cations, and all anions were chelated with chloride ions. The chemical species comprising each precursor were standardized for two reasons. First, to enhance the solubility of the precursors. Second, to ensure uniformity in the effect of each ion on the synthesis process across all samples. The mixture was added in a dropwise manner by a syringe pump (NE-300, New Era Pump Systems, Inc.) at a speed of 2 mL/min. The solution turned into black and cooled to room temperature naturally. PHEA nanoparticles were precipitated by using a mixture of ether and acetone (ether : acetone : PHEA solution = 20 : 10 : 5, v/v) and washed several times with a mixture of ethanol, acetone and ether to remove excess surfactant (PVP) and solvent (TEG).

This article is protected by copyright. All rights reserved.

Author Manuscript

Peroxidase-like activity measurement of PHEA, DHEA and Mono Pt: The samples' peroxidase-like performance was evaluated in a 0.1 M phosphate buffer (25 °C, pH 6.0) across diverse concentrations. H_2O_2 (258 µL, 35 wt%) and TMB (50 µL, 2.5 mg/mL in dimethylsulfoxide) were used, both in amounts surpassing saturation requirements. The nanozyme catalysts' concentrations ranged from 5 × 10^{-5} to 2.5 ×10^{-4} mmol, with a 1.67 µM solution to achieve a final reaction volume of 1 mL. The samples' enzyme kinetics involving TMB and H_2O_2 were analyzed for the kinetic assays. Using GraphPad Prism version 7 software, the Michaelis–Menten equation was fitted to the data to obtain kinetic parameters. The V_{max}/[E] calculation yielded the k_{cat} value.

Catalase-like activity measurement of PHEA, DHEA: The catalase-like (CAT) activity of nanozymes was evaluated using two methods. Firstly, the oxygen generated from the decomposition of H_2O_2 was measured using a dissolved oxygen meter. Different concentrations of nanozymes (20–180 µL, 1 mg/mL) were mixed with H_2O_2 (20 µL, 50

This article is protected by copyright. All rights reserved.

Author Manuscript

mM) in 20.0 mL of phosphate buffer (0.1 M, pH 6). Secondly, the decomposition of H_2O_2 was monitored with a UV spectrophotometer. In a typical procedure, nanozyme samples (200 µL, 10 µg/mL) and H_2O_2 solution (800 µL, 10 mM in 0.1 M phosphate buffer, pH 6.0) were combined in a cuvette, and the absorbance change at 240 nm was continuously recorded at 25°C for 10 minutes. The specific catalase activity of the nanozyme samples was determined based on a classical UV assay with slight modifications.

Evaluation of Extracellular RONS and extracellular pro-inflammatory cytokine level:

To measure extracellular RONS levels, at a density of 1×10^5 cells per well, RAW 264.7 cells were seeded on a 24-well plate and incubated in Dulbecco's modified Eagle's medium (DMEM) with 10 v/v% fetal bovine serum (FBS), 1 v/v% penicillin, and streptomycin at 37°C. After incubation for 24 h, the media was replaced with fresh media containing 5 µg mL^{-1} LPS and sample (PBS or 200 µg mL^{-1} PHEA). After incubation for 24

This article is protected by copyright. All rights reserved.

Author Manuscript

h, the supernatant was obtained by collecting and centrifuging the media (3,000 rpm, 10 min, 4°C).

Each supernatant was transferred to 96-well plate and the amount of ROS and NO in supernatant was quantified by Amplex red assay and Griess assay according to the manufacturer's protocol, respectively. The concentration of the extracellular pro-inflammatory cytokines in the supernatant was similarly measured using mouse IL-6 and mouse TNF-α ELISA, following the manufacturer's protocol.

Animal experiments:

All animal experiments were performed under the guide lines from the POSTECH Institutional Animal Care and Use Committee (IACUC) under POSTECH Biotech Center Ethics Committee (POSTECH-2024-0010). C57BL/6 mice (female, 6 weeks old) were purchased from Hana Bio (Gyeonggi, Korea).

This article is protected by copyright. All rights reserved.

Author Manuscript

In vivo peritonitis model:

100 μL of sample (DPBS or 5 mg kg^{-1} PHEA nanozyme) was intravenously injected into 6-week-old female C57BL/6 mice. After 30 min, LPS (10 mg kg^{-1}) was intraperitoneally injected into the C57BL/6 mice to induce peritonitis model. The mice were anesthetized, and 2 mL of cold PBS was injected into the peritoneum 4 hours after LPS injection. The mice were gently shaken, and peritoneal lavage (>1.5 mL) was collected. At the same time, whole blood was obtained by heart puncture and serum was obtained by centrifugation at 3,000 rpm, 4°C for 15 min. The ROS and NO levels of the peritoneal fluid and serum were quantified by Amplex red assay and Griess assay according to the manufacturer's protocol, respectively. The cytokine levels including IL-6 and TNF-alpha of the peritoneal fluid and serum were measured by ELISA according to the manufacturer's protocol. To evaluate the level of liver injury, the mice were sacrificed 12 h after LPS

This article is protected by copyright. All rights reserved.

Author Manuscript

injection and serum were obtained for biochemical analysis (ALT and AST assay). Meanwhile, liver tissues were also collected for histopathological analysis.

More details about chemicals, instruments, DHEA and Mono nanozymes synthesis, SOD-like activity, HORAC, NO scavenging, Cell viability test, Imaging of intracellular ROS and NO level and Hemolysis test are listed in the Supporting information.

Supporting Information

Supporting Information is available from the Wiley Online Library or from the author.

Acknowledgements

D.C., Y.B., S.P. and L.X. contributed equally to this work. This study was supported by the National Research Foundation of Korea (NRF) Grant (NRF-2022R1A3B1077354, RS-2023-

This article is protected by copyright. All rights reserved.

00235596 and RS-2024-00335715) funded by the Korea government (Ministry of Science and ICT).

Received: ((will be filled in by the editorial staff))

Revised: ((will be filled in by the editorial staff))

Published online: ((will be filled in by the editorial staff))

References

[1] S. Di Meo, T. T. Reed, P. Venditti, V. M. Victor, Oxid. Med. Cell. Longev. 2016, 2016, 1245049.

[2] C. Lennicke, H. M. Cochemé, Mol. Cell 2021, 81, 3691.

[3] F. Ursini, M. Maiorino, H. J. Forman, Redox Biol. 2016, 8, 205.

This article is protected by copyright. All rights reserved.

Author Manuscript

Author Manuscript

[4] a) H. J. Kwon, D. Kim, K. Seo, Y. G. Kim, S. I. Han, T. Kang, M. Soh, T. Hyeon, Angew. Chem. Int. Ed. 2018, 57, 9408; b)Y. Liu, Y. Cheng, H. Zhang, M. Zhou, Y. Yu, S. Lin, B. Jiang, X. Zhao, L. Miao, C.-W. Wei, Q. Liu, Y.-W. Lin, Y. Du, C. J. Butch, H. Wei, Sci. Adv. 2020, 6, eabb2695; c)Y. Zhao, S. Song, D. Wang, H. Liu, J. Zhang, Z. Li, J. Wang, X. Ren, Y. Zhao, Nat. Commun. 2022, 13, 6758.

[5] a)R. Zhang, B. Xue, Y. Tao, H. Zhao, Z. Zhang, X. Wang, X. Zhou, B. Jiang, Z. Yang, X. Yan, K. Fan, Adv. Mater. 2022, 34, 2205324; b) W. Gao, J. He, L. Chen, X. Meng, Y. Ma, L. Cheng, K. Tu, X. Gao, C. Liu, M. Zhang, K. Fan, D.-W. Pang, X. Yan, Nat. Commun. 2023, 14, 160; c) H. Zhang, P. Wang, J. Zhang, Q. Sun, Q. He, X. He, H. Chen, H. Ji, Angew. Chem. Int. Ed. 2024, 63, e202316779.

[6] a) Y. Yao, Q. Dong, A. Brozena, J. Luo, J. Miao, M. Chi, C. Wang, I. G. Kevrekidis, Z. J. Ren, J. Greeley, G. Wang, A. Anapolsky, L. Hu, Science 2022, 376, eabn3103;

b) K. Li, W. Chen, Mater. Today Energy 2021, 20, 100638; c) N. Kumar Katiyar, K. Biswas, J.-W. Yeh, S. Sharma, C. Sekhar Tiwary, Nano Energy 2021, 88, 106261.

This article is protected by copyright. All rights reserved.

Author Manuscript

[7] a) T. Löffler, A. Ludwig, J. Rossmeisl, W. Schuhmann, Angew. Chem. Int. Ed. 2021, 60, 26894; b) S. Schweidler, M. Botros, F. Strauss, Q. Wang, Y. Ma, L. Velasco, G. Cadilha Marques, A. Sarkar, C. Kübel, H. Hahn, J. Aghassi-Hagmann, T. Brezesinski, B. Breitung, Nat. Rev. Mater. 2024, 9, 266.

[8] Y.-H. Liu, C.-J. Hsieh, L.-C. Hsu, K.-H. Lin, Y.-C. Hsiao, C.-C. Chi, J.-T. Lin, C.-W. Chang, S.-C. Lin, C.-Y. Wu, J.-Q. Gao, C.-W. Pao, Y.-M. Chang, M.-Y. Lu, S. Zhou, T.-H. Yang, Sci. Adv. 2023, 9, eadf9931.

[9] a) J. Qiu, Q. N. Nguyen, Z. Lyu, Q. Wang, Y. Xia, Adv. Mater. 2022, 34, 2102591; b) P. Mélinon, S. Begin-Colin, J. L. Duvail, F. Gauffre, N. H. Boime, G. Ledoux, J. Plain, P. Reiss, F. Silly, B. Warot-Fonrose, Phy. Rep. 2014, 543, 163.

[10] A. B. Yankovich, B. Berkels, W. Dahmen, P. Binev, S. I. Sanchez, S. A. Bradley, A. Li, I. Szlufarska, P. M. Voyles, Nat. Commun. 2014, 5, 4155.

[11] a) K. D. Gilroy, X. Yang, S. Xie, M. Zhao, D. Qin, Y. Xia, Adv. Mater. 2018, 30, 1706312; b) N. C. Bigall, T. Härtling, M. Klose, P. Simon, L. M. Eng, A. Eychmüller,

This article is protected by copyright. All rights reserved.

Author Manuscript

Nano Lett. 2008, 8, 4588. c)X. Xia, S. Xie, M. Liu, H.-C. Peng, N. Lu, J. Wang, M. J. Kim, Y. Xia, Proc. Natl. Acad. Sci. 2013, 110, 6669.

[12] C. Song, A. Yang, O. Sakata, L. S. R. Kumara, S. Hiroi, Y.-T. Cui, K. Kusada, H. Kobayashi, H. Kitagawa, Phys. Chem. Chem. Phys. 2018, 20, 15183.

[13] D. Wu, K. Kusada, Y. Nanba, M. Koyama, T. Yamamoto, T. Toriyama, S. Matsumura, O. Seo, I. Gueye, J. Kim, L. S. Rosantha Kumara, O. Sakata, S. Kawaguchi, Y. Kubota, H. Kitagawa, J. Am. Chem. Soc. 2022, 144, 3365.

[14] T. Xia, K. Zhao, Y. Zhu, X. Bai, H. Gao, Z. Wang, Y. Gong, M. Feng, S. Li, Q. Zheng, S. Wang, R. Wang, H. Guo, Adv. Mater. 2023, 35, 2206508.

[15] Q. Jia, N. Ramaswamy, H. Hafiz, U. Tylus, K. Strickland, G. Wu, B. Barbiellini, A. Bansil, E. F. Holby, P. Zelenay, S. Mukerjee, ACS Nano 2015, 9, 12496.

[16] G. Feng, Y. Pan, D. Su, D. Xia, Adv. Mater. 2024, 36, 2309715.

This article is protected by copyright. All rights reserved.

Author Manuscript

[17] B. Wang, Y. Fang, X. Han, R. Jiang, L. Zhao, X. Yang, J. Jin, A. Han, J. Liu, Angew. Chem. Int. Ed. 2023, 62, e202307133.

[18] X. Zhang, Q. Yang, Y. Lang, X. Jiang, P. Wu, Anal. Chem. 2020, 92, 12400.

[19] a) X. Shen, Z. Wang, X. Gao, Y. Zhao, ACS Catal. 2020, 10, 12657; b) I. E. L. Stephens, A. S. Bondarenko, U. Grønbjerg, J. Rossmeisl, I. Chorkendorff, Energy Environ. Sci. 2012, 5, 6744.

[20] B. Jiang, D. Duan, L. Gao, M. Zhou, K. Fan, Y. Tang, J. Xi, Y. Bi, Z. Tong, G. F. Gao, N. Xie, A. Tang, G. Nie, M. Liang, X. Yan, Nat. Protoc. 2018, 13, 1506.

[21] a) F. H. B. Lima, J. Zhang, M. H. Shao, K. Sasaki, M. B. Vukmirovic, E. A. Ticianelli, R. R. Adzic, J. Phys. Chem. C 2007, 111, 404; b)Z. Xi, K. Wei, Q. Wang, M. J. Kim, S. Sun, V. Fung, X. Xia, J. Am. Chem. Soc. 2021, 143, 2660.

[22] a) C. Li, Q. Yuan, B. Ni, T. He, S. Zhang, Y. Long, L. Gu, X. Wang, Nat. Commun. 2018, 9, 3702; b) B. Lim, M. Jiang, P. H. C. Camargo, E. C. Cho, J. Tao, X. Lu, Y.

This article is protected by copyright. All rights reserved.

Zhu, Y. Xia, Science 2009, 324, 1302; c)H. Tan, J. Kim, J. Lin, C. Li, S. M. Alsheri, T. Ahamad, N. Alhokbany, Y. Bando, M. Zaman, M. S. A. Hossain, S. Wang, Y. Yamauchi, Microporous and Mesoporous Mater. 2019, 280, 1.

[23] M. Kim, M. S. Kim, S. H. Kweon, S. Jeong, M. H. Kang, M. I. Kim, J. Lee, J. Doh, Adv. Healthc. Mater. 2015, 4, 1311.

[24] D. K. Tiwari, T. Jin, J. Behari, Toxicol. Mech. Methods 2011, 21, 13.

[25] J. Kim, H. Y. Kim, S. Y. Song, S.-h. Go, H. S. Sohn, S. Baik, M. Soh, K. Kim, D. Kim, H.-C. Kim, N. Lee, B.-S. Kim, T. Hyeon, ACS Nano 2019, 13, 3206.

[26] a) J. C. Barreto, G. S. Smith, N. H. P. Strobel, P. A. McQuillin, T. A. Miller, Life Sci. 1994, 56, PL89; b) Y. Zhu, W. Wang, J. Cheng, Y. Qu, Y. Dai, M. Liu, J. Yu, C. Wang, H. Wang, S. Wang, C. Zhao, Y. Wu, Y. Liu, Angew. Chem. Int. Ed. 2021, 60, 9480.

[27] T. Kim, J. Suh, W. J. Kim, Adv. Mater. 2021, 33, 2008793.

Author Manuscript

This article is protected by copyright. All rights reserved.

Author Manuscript

[28] a) C. Bogdan, Nat. Immunol. 2001, 2, 907; b) J. N. Sharma, A. Al-Omran, S. S. Parvathy, Inflammopharmacology 2007, 15, 252.

[29] B. Halliwell, Biochem. Soc. Trans. 2007, 35, 1147.

[30] P.-F. Wang, K. Xie, Y.-X. Cao, A. Zhang, Mediators Inflamm., 2022 , 6394199.

[31] D. Wu, K. Kusada, T. Yamamoto, T. Toriyama, S. Matsumura, S. Kawaguchi, Y. Kubota, H. Kitagawa, J. Am. Chem. Soc. 2020, 142, 13833.

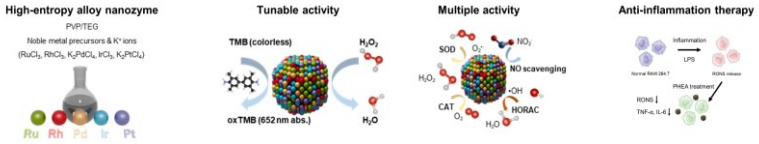
In this study, the synthesis of ultra-small HEA nanozymes with precisely tunable morphology and multifaceted catalytic activities for efficient ROS scavenging is presented. The HEA nanozymes demonstrated a 5.2-fold increase in peroxidase (k_{cat}/K_M) activity, alongside catalytic functionalities including a superoxide dismutase-catalase cascade reaction, •OH, and NO scavenging, resulting in superior *in vitro* and *in vivo* anti-inflammatory efficacy.

This article is protected by copyright. All rights reserved.

Author Manuscript

Daeeun Choi, Yeonju Boo, Seonhye Park, Liangliang Xu, Seongbeen Kim, Seung Yeop Yi, Sangmin Lee, Ruopeng Wu, Won Jong Kim and Jinwoo Lee**

Ultrasmall High-Entropy-Alloy Nanozyme Catalyzed *In Vivo* ROS and NO Scavenging for Anti-Inflammatory Therapy



This article is protected by copyright. All rights reserved.